High-Efficiency and Full-Space Manipulation of Electromagnetic Wave Fronts with Metasurfaces

Tong Cai,[1,2] GuangMing Wang,[2] ShiWei Tang,[3] HeXiu Xu,[1,2] JingWen Duan,[4] HuiJie Guo,[1] FuXin Guan,[1] ShuLin Sun,[4] Qiong He,[1,5,*] and Lei Zhou[1,5,†]

[1]*State Key Laboratory of Surface Physics, Key Laboratory of Micro and Nano Photonic Structures (Ministry of Education), and Department of Physics, Fudan University, Shanghai 200433, China*
[2]*Air and Missile Defend College, Air Force Engineering University, Xi'an 710051, China*
[3]*Department of Physics, Faculty of Science, Ningbo University, Ningbo 315211, China*
[4]*Shanghai Engineering Research Center of Ultra-Precision Optical Manufacturing, Green Photonics and Department of Optical Science and Engineering, Fudan University, Shanghai 200433, China*
[5]*Collaborative Innovation Center of Advanced Microstructures, Nanjing 210093, China*

(Received 6 July 2017; published 28 September 2017)

Metasurfaces offer great opportunities to control electromagnetic (EM) waves, but currently *most* metadevices work either in *pure reflection* or *pure transmission* mode, leaving half of the EM space completely unexplored. Here, we propose an alternative type of metasurface, composed of specifically designed meta-atoms with polarization-dependent transmission and reflection properties, to efficiently manipulate EM waves in the full space. As a proof of concept, three microwave metadevices are designed, fabricated, and experimentally characterized. The first two metadevices can bend or focus EM waves at different sides (i.e., transmission and reflection sides) of the metasurfaces, depending on the incident polarization, while the third one changes from a wave bender for the reflected wave to a focusing lens for the transmitted wave as the excitation polarization is rotated, with all of these functionalities exhibiting very high efficiencies (in the range of 85%–91%) and total thickness $\sim\lambda/8$. Our findings significantly expand the capabilities of metasurfaces in controlling EM waves, and can stimulate high-performance multifunctional metadevices facing more challenging and diversified application demands.

DOI: 10.1103/PhysRevApplied.8.034033

I. INTRODUCTION

As the basis of nearly all optical devices, manipulating the electromagnetic (EM) wave front as desired is crucial in modern photonic research. Natural materials exhibit limited variation ranges of permittivity and permeability, so that EM devices made by them are typically too bulky in size and of restricted functionalities, both being unfavorable for EM integration [1–3]. Recently, metamaterials (artificial materials made by subwavelength microstructures with tailored EM properties), and particularly their planar version, metasurfaces, have demonstrated strong capabilities to manipulate EM waves, generating many fascinating effects such as anomalous refraction and reflection [4–6], propagating-wave-to-surface-wave coupling [7–10], planar holograms [11–13], focusing lenses [14–18], photonic spin Hall effects [19–21], and many others [22–40]. These powerful wave-manipulation abilities have led to many metasurface-based functional EM devices [14,25,28–30,41–45], which are usually thin, flat, and exhibit diversified and multiple functionalities, all being very promising for modern integration-optics applications.

Despite the great successes achieved so far, we note that the wave-manipulation capabilities of metasurfaces are far less explored, which also limits the application potentials of them. For example, high-efficiency metasurfaces usually work either in *pure reflection mode* [4–6,20–24] [see Fig. 1(a)] or *pure transmission mode* [24–28,36,38,42], which means that they can only efficiently manipulate either the reflected wave front or transmitted one, leaving half of the EM space totally unutilized. While some metasurfaces could, in principle, control the wave fronts of both transmitted and reflected waves [5,6,38,39], the phase gradients provided for transmitted and reflected waves are usually identical, leading to locked wave-manipulation functionalities at two sides of the metasurfaces, not mentioning the low efficiencies of these devices due to the undesired multimode generations [see Fig. 1(b)]. Although many multifunctional metasurface-based devices have been proposed, they typically integrate different functionalities working for either transmission or reflection mode [24,28], not for both. It is highly desired to expand the wave-manipulation capabilities of metasurfaces to the full EM space, offering the metasurfaces independently controlled functionalities at their two different sides.

*Corresponding author.
qionghe@fudan.edu.cn
†Corresponding author.
phzhou@fudan.edu.cn

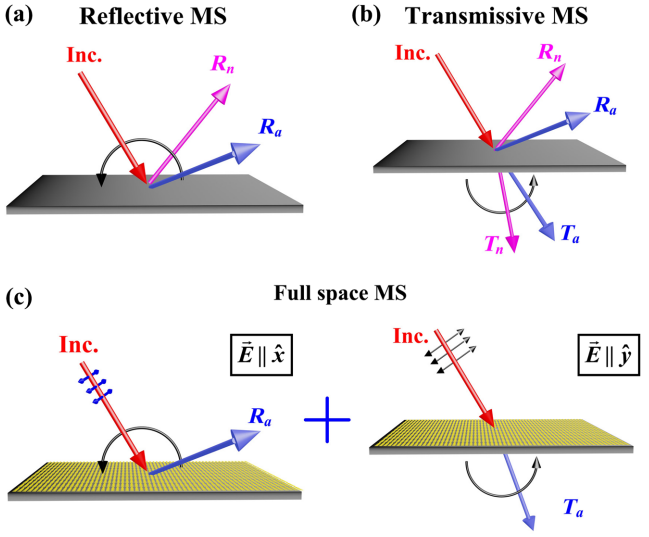

FIG. 1. Working principle and advantages of the full-space metasurface. Conventional metasurfaces working in (a) reflection or (b) transmission geometries suffer from the issues of restricted working space, low efficiency due to multimode generations, and locked phase gradients for transmitted and reflected waves. (c) The proposed full-space metasurface can efficiently manipulate electromagnetic wave fronts at both sides of the device with independent functionalities, triggered by incident waves with different polarizations.

In this paper, we propose an alternative strategy to design metasurfaces that can manipulate the wave fronts of EM waves in *full space* and with very *high efficiencies* [see Figs. 1(c) and 1(d)]. The key step is to design a collection of meta-atoms which are perfectly transparent or reflective for incident waves polarized along two orthogonal directions, yet exhibiting tailored (transmission and reflection) phases covering the whole 360° range. We can thus utilize this set of meta-atoms to construct metasurfaces to efficiently and independently control the wave fronts of EM waves at different sides of the metasurfaces, dictated by the incident polarization. As a proof of concept, we experimentally realize three microwave metasurfaces: the first two can bend or focus EM waves at two sides of the metasurfaces, while the third one combines the functionalities of wave bending (for reflected wave) and focusing (for transmitted wave) into one single device. In particular, all of these devices exhibit very high working efficiencies for all functionalities (in the range of 85%–91%) with total thickness $\sim\lambda/8$. Our findings offer possibilities to realize high-efficiency multifunctional metadevices working in the full space, which can lead to many exciting applications in different frequency domains.

II. CONCEPT AND META-ATOM DESIGN

We describe our strategy to realize the full-space wavefront control on the EM wave, starting from discussing how to design appropriate meta-atoms. Consider a meta-atom exhibiting mirror symmetry, then its EM characteristics can be described by two diagonal Jones matrices $R = \left(\begin{smallmatrix} r_{xx} & 0 \\ 0 & r_{yy} \end{smallmatrix}\right)$ and $T = \left(\begin{smallmatrix} t_{xx} & 0 \\ 0 & t_{yy} \end{smallmatrix}\right)$, with r_{xx}, r_{yy}, t_{xx}, and t_{yy} denoting the reflection and transmission coefficients for waves polarized along two principal axes $\hat{x}$ and $\hat{y}$. In lossless systems, we have $|r_{xx}|^2 + |t_{xx}|^2 = 1$ and $|r_{yy}|^2 + |t_{yy}|^2 = 1$ due to the energy conservation. To achieve independent yet highly efficient controls on both transmitted and reflected waves, we require our meta-atoms to be perfectly reflective for the $\hat{x}$-polarized incident wave (i.e., $|t_{xx}| = 0, |r_{xx}| = 1$), and perfectly transparent for the $\hat{y}$-polarized incident wave (i.e., $|t_{yy}| = 1, |r_{yy}| = 0$). Moreoever, the phases associated with their two nonzero coefficients r_{xx} and t_{yy}, denoted by φ^r_{xx} and φ^t_{yy}, respectively, can be freely tuned by varying the structural details of the meta-atoms. If these meta-atoms can be designed, we can thus ultilize them to construct a metasurface exhibiting the desired phase distributions [i.e., $\varphi^r_{xx}(x, y)$ and $\varphi^t_{yy}(x, y)$] to realize certain predetermined functionalities for controlling reflected and transmitted wave fronts, under $\hat{x}$- and $\hat{y}$-polarized excitations, respectively.

Figure 2(a) shows the designed meta-atom that can exhibit the mentioned polarization-dependent EM characteristics. As shown in the inset to Fig. 2(a), the meta-atom consists of four metallic layers separated by three 1.5-mm-thick F4B dielectric spacers (with $\varepsilon_r = 2.65 + 0.01i$). The first two layers are ansiotropic metallic crosses consisting of two metallic bars with lengths carefully adjusted, while the bottom two layers are topologically different, which are *continuous* metallic stripes (along the x direction) decorated with small perpendicular metallic bars (along the y direction). Now, the advantages of design are clear. Those x-orientated continuous metallic stripes on the bottom two layers essentially work as an *effective optical grating* to efficiently block the $\hat{x}$-polarized wave and leave only the $\hat{y}$-polarized waves to pass through, in the frequency regime (around 10 GHz) studied in this paper. The roles of the top two metallic crosses are to further tune the phases and amplitudes of the transmitted and reflected waves, for two different polarizations. Consider first the $\hat{x}$ polarization. The coupling between top metallic resonators with the bottom continuous stripes generates two magnetic resonances, which can dramatically change the reflection phase as a function of frequency. Figure 2(c) depicts the simulated spectra of the reflection amplitude and phase of a typical meta-atom (periodically replicated) under $\hat{x}$-polarization excitation. Indeed, within the frequency interval (7–13 GHz) of interest, our meta-atom can nearly totally reflect the $\hat{x}$-polarized wave with reflection-phase φ^r_{xx} varying from −180° to 180° as frequency passes through the magnetic resonance at 9.1 GHz [8,22,23]. In this particular example, only one magnetic resonance appears since the bar in the second layer is also continuous ($d_2 = 11$ mm), which does not generate a resonance.

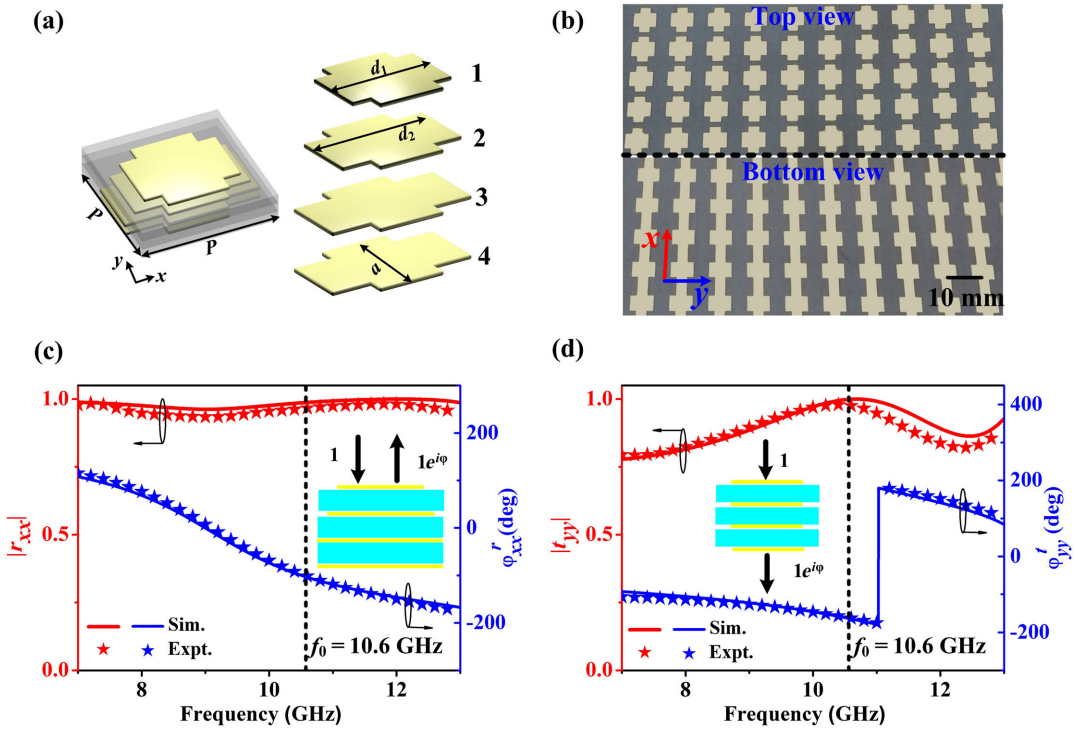

FIG. 2. Design and characterization of the proposed meta-atom. (a) Schematics of the proposed meta-atom composed by four metallic layers separated by three F4B spacers ($\varepsilon_r = 2.65 + 0.01i$, $h = 1.5$ mm). The following geometrical parameters are fixed: width of each y-orientated bar is $w_1 = 5$ mm, width of each x-orientated bar or stripe is $w_2 = 4$ mm, lengths of the x-orientated stripes in the third and fourth layers are fixed to the periodicity $d_3 = d_4 = P = 11$ mm. Other parameters (d_1, d_2 and lengths of all y-orientated bars a) are tuned appropriately in designing each meta-atom. (b) Top- and bottom-view pictures of a fabricated metasurface consisting of a periodic array of meta-atoms with $a = 6.3$ mm, $d_1 = 9$ mm, and $d_2 = 11$ mm. Measured and FDTD simulated amplitude-phase spectra of reflection (c) and transmission (d) for the periodic metasurface under excitations with different polarizations.

Two magnetic resonances can appear if the bar in the second layer also exhibits a finite length (i.e., $d_2 < 11$ mm). Therefore, we can have an expanded freedom to design our meta-atom by setting both d_1 and d_2 freely adjustable (see Sec. A of the Supplemental Material [46]). For the $\hat{y}$ polarization, however, EM waves can only "see" the y-orientated metallic bars in each layer. Since all y-orientated metallic bars are of short lengths, their Lorentz resonances are at frequencies much higher than the frequency region that we are interested in, and therefore, EM waves of this polarization can easily pass through each layer. The coupling between different layers can further enhance the transmission by forming a series of Fabry-Perot transmission modes (see Supplemental Material, Sec. A [46]). Via adjusting the geometrical parameters, we can appropriately cascade the generated transmission resonances to get a wideband transparent window with a controllable transmission phase. Figure 2(d) shows the simulated spectra of transmission amplitude $|t_{yy}|$ and phase φ^t_{yy} for a typical sample, where we find that $|t_{yy}| > 0.84$ within the frequency band 7–13 GHz, while the variation range of φ^t_{yy} can cover the whole 360° range.

We fabricate a microwave sample (with a size of 330 mm × 330 mm) consisting of a *periodic* array of a typical meta-atom. Figure 2(b) shows the top-view and bottom-view pictures of the sample. We then experimentally characterize its transmission and reflection characteristics, and compare the measured results with the simulated spectra based on finite-difference-time-domain (FDTD) simulations in Figs. 2(c) and 2(d). Excellent agreement is noted between measured and simulated spectra.

Figure 2 illustrates that such a meta-atom structure is an ideal building block to construct our metasurfaces to achieve the full-space wave-front control. Now that the reflection and transmission phases (φ^r_{xx} and φ^t_{yy}) are dictated by the magnetic resonances (for $\hat{x}$ polarization) and the transmission resonances (for $\hat{y}$ polarization), respectively, we understand that changing the geometric structural details of our meta-atom can significantly tune the two phases via varying the corresponding resonance-mode positions. In addition, we understand that these geometrical parameters have different roles in affecting the two phases. Obviously, structural parameters d_1, d_2 are mainly responsible for φ^r_{xx}, while the parameter a mainly changes φ^t_{yy}. These nearly delinked control abilities make our realistic design relatively easy, and we can design metasurfaces with arbitrary distributions of $\varphi^r_{xx}(x, y)$ and $\varphi^t_{yy}(x, y)$ according to their desired functionalities, via

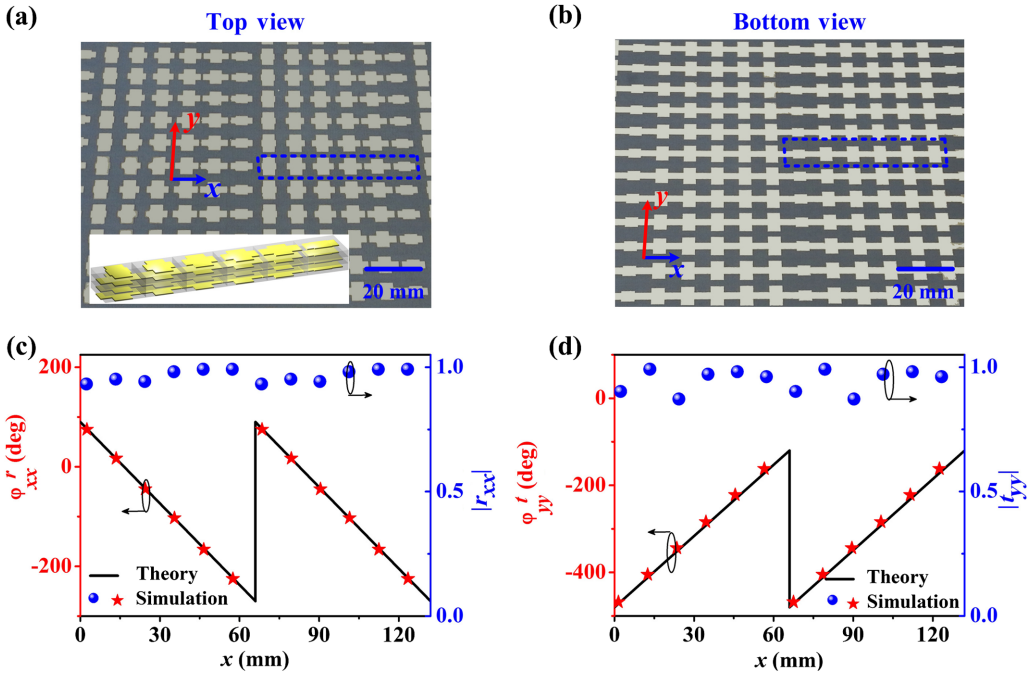

FIG. 3. Design and fabrication of the full-space beam deflector. (a) Top-view and (b) bottom-view pictures of the fabricated full-space beam deflector. FDTD simulated profiles of (c) $\varphi^r_{xx}(x)$, $|r_{xx}(x)|$, (d) φ^t_{yy}, and $|t_{yy}|$ for the designed full-space beam deflector, compared with the theoretically requested lines $\varphi^r_{xx} = C_0 - 0.43k_0x$ and $\varphi^t_{yy} = C_1 + 0.43k_0x$ (black lines). Here, the working frequency is $f_0 = 10.6$ GHz.

choosing meta-atoms with carefully adjusted geometrical parameters based on the parameter maps recorded in the Supplemental Material, Sec. B [46]. We note that in adjusting these geometrical parameters, the reflection and transmission amplitudes of the meta-atoms $|r_{xx}(x,y)|$ and $|t_{yy}(x,y)|$ can remain at very high values, which ensure the high efficiency of the realized functionality (see Supplemental Material, Sec. B [46]). We note that our mechanism is obviously different from previous attempts of making multifunctional devices, exploring only half of the EM space [12,14,15,21,24–27], and those attempts utilizing the full EM space but exhibiting locked and low-efficiency functionalities [4,5,38,39]. In the following sections, we will discuss several examples to illustrate our concept.

III. EXPERIMENTAL RESULTS AND DISCUSSIONS

A. Full-space beam deflector

As the first example, we employ our meta-atoms to design a high-efficiency beam deflector working in the full space. To achieve this goal, we require that φ^r_{xx} and φ^t_{yy} exhibit the following distributions:

$$\varphi^r_{xx} = C_0 + \xi_1 x, \qquad \varphi^t_{yy} = C_1 + \xi_2 x, \tag{1}$$

where C_0 and C_1 are two constants, and ξ_1 and ξ_2 are two phase gradients which determine the bending angles of the anomalously reflected and refracted beams, respectively [4–7]. Setting the working frequency as $f_0 = 10.6$ GHz, we choose six meta-atoms to form a supercell for our metasurface, and then optimize their geometrical parameters to make Eq. (1) satisfied with $\xi_1 = -0.43k_0$ and $\xi_2 = 0.43k_0$, where $k_0 = 2\pi f_0/c$, with c being the speed of light. The structural details of the optimized meta-atoms are summarized in Sec. C of the Supplemental Material [46]. To validate our design, we depict in Figs. 3(c)–3(d) the FDTD simulated distributions of the reflection-transmission amplitude and phase of the designed metasurface. We find that the two phase distributions match well with the theoretical curves. Meanwhile, these meta-atoms exhibit competitive values of transmission-reflection amplitudes ($|r_{xx}| > 0.93$ and $|t_{yy}| > 0.86$), which can guarantee the high-efficiency operations of our metadevices.

We fabricate a metasurface sample according to the design [see Figs. 3(a) and 3(b) for its top-view and bottom-view pictures], which contains 30×30 meta-atoms with a total size of 330×330 mm^2, and then experimentally characterized its wave-manipulation performances. We first characterize the $\hat{x}$-polarization properties of the metasurface. Shining an $\hat{x}$-polarized microwave normally onto our metasurface, we measure the angular distributions of scattered waves at both reflection and transmission sides of the metasurface. As shown in Figs. 4(a) and 4(b), within a frequency interval (10.35 to 11.15 GHz), most input power is reflected to an oblique angle determined by the generalized Snell's law $\theta_r = \sin^{-1}(\xi_1/k_0)$ [solid stars in Fig. 4(a)] [4–7]. The best performance appears at 10.6 GHz where all undesired modes in the full space are suppressed, leaving only the anomalous reflection surviving. This already implies the good working efficiency of our device. We next characterize the $\hat{y}$-polarization properties of the metasurface following the same procedures. Figures 4(d) and 4(e) show, respectively, the measured angular power distributions of the scattered waves in reflection and

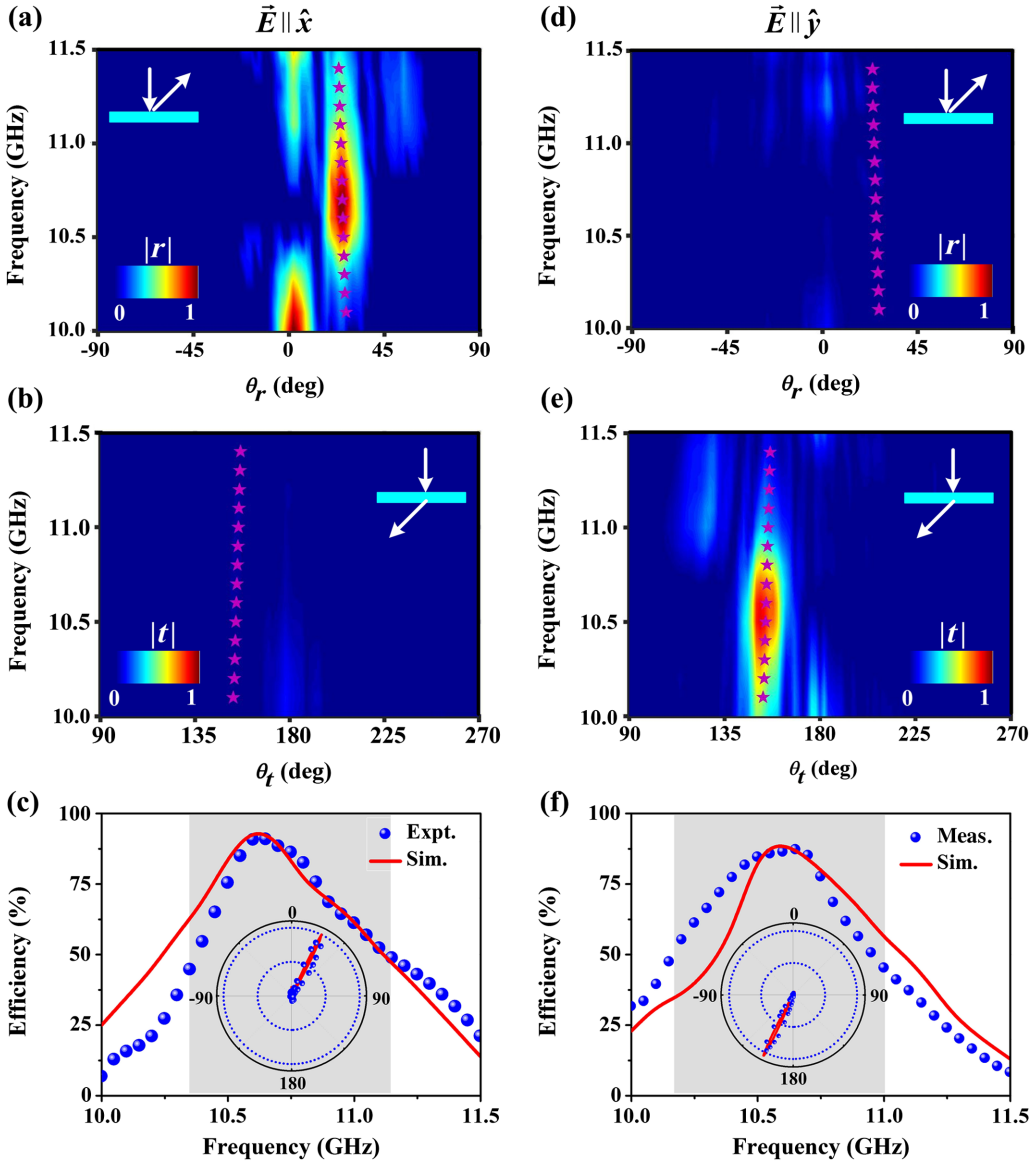

FIG. 4. Characterizations of the full-space beam deflector under normal incidence. Measured scattered-field intensity (color map) versus frequency and detecting angle at (a) reflection and (b) transmission sides of the metasurface shined by $\hat{x}$-polarized microwaves. (c) Simulated and measured absolute efficiencies of the reflective beam-bending functionality of the device. Measured scattered-field intensity (color map) versus frequency and detecting angle at (d) reflection and (e) transmission sides of the metasurface shined by $\hat{y}$-polarized microwaves. (f) FDTD simulated and measured absolute efficiencies of the transmissive beam-bending functionality of the device. Insets to (c) and (f) depict the measured (symbols) and simulated scattering patterns of our metasurface illuminated by $\hat{x}$- and $\hat{y}$-polarized waves, respectively, at the frequency $f_0 = 10.6$ GHz. All signals are normalized against a reference value obtained by replacing the metadevice with a metallic plate of the same size.

transmission sides for our metasurface under the illumination of the $\hat{y}$-polarized wave. As expected, within the frequency interval (10.2 to 11.0 GHz), most input power is now redirected to the *transmission* channel at the angle determined by the generalized Snell's law $\theta_t = \sin^{-1}(\xi_2/k_0)$ [solid stars in Fig. 4(e)], with the best performance again appearing at the working frequency 10.6 GHz.

We quantitatively characterize the working efficiencies of our device. At each frequency, we compute the working efficiency as the ratio between the power carried by the desired anomalously deflected mode (either at the reflection or transmission side) and a reference value representing the total power carried by the input beam [8,20,24]. The former value is obtained by integrating over an appropriate angle region occupied by the desired mode, while the reference is obtained via integrating over the angle region of the specularly reflected mode when the metasurface is replaced by a metallic plate of the same size (see Sec. E of the Supplemental Material for more details [46]). Figures 4(c) and 4(f) depict the working efficiencies of our device [retrieved from the experimental data shown in Figs. 4(a) and 4(b), as well as Figs. 4(d) and 4(e)] as functions of frequency, for two polarization-dependent functionalities. We also perform FDTD simulations to compute the angular distributions of the scattering patterns at each frequency for two polarizations (see Supplemental Material, Sec. *D* [46]), from which we successfully obtain the theoretical values of working efficiencies for our device. As shown in Figs. 4(c) and 4(f), the experimentally retrieved efficiencies match well with their corresponding theoretical ones. In particular, our experiments indicate that the working efficiencies of the fabricated device can be as high as 91% (reflection side) and 85% (transmission side), while these values are 93% and 88% estimated from FDTD simulations. The slight difference between the measured

and simulated results can be attributed to inevitable fabrication errors and imperfections of the incoming wave fronts generated by our microwave horns.

B. Full-space metalens

As another example, we design a full-space metalens, which can focus EM waves at its reflection and transmission sides for $\hat{x}$- and $\hat{y}$-polarized incident waves, respectively [see Figs. 5(a) and 5(e)]. To achieve this end, the two phase functions (φ^r_{xx} and φ^t_{yy}) of our metadevice should exhibit the following distributions:

$$\varphi^r_{xx}(x,y) = k_0\left(\sqrt{F_1^2 + x^2 + y^2} - F_1\right),$$
$$\varphi^t_{yy}(x,y) = k_0\left(\sqrt{F_2^2 + x^2 + y^2} - F_2\right), \quad (2)$$

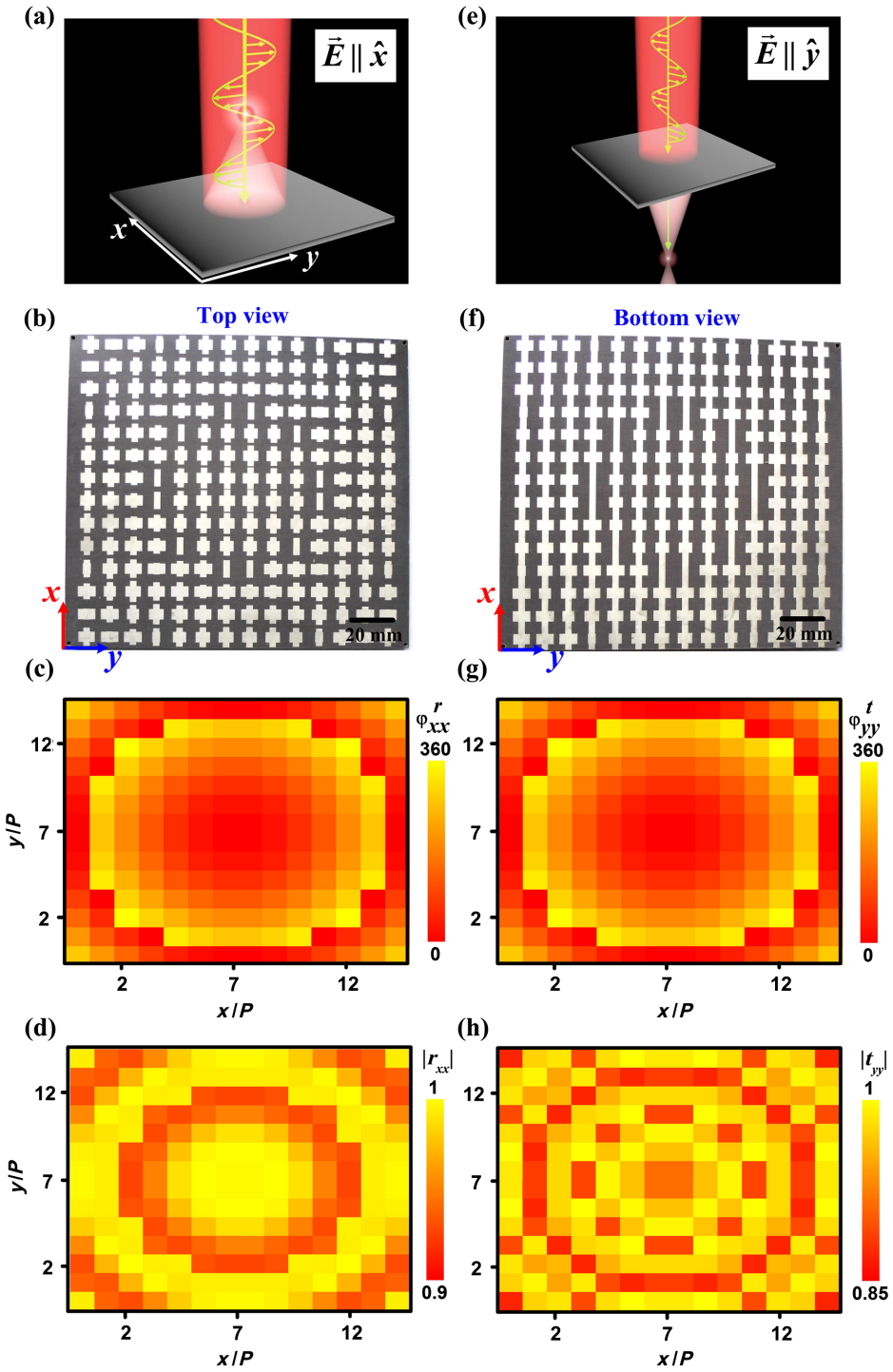

FIG. 5. Design and sample of the full-space metalens. Schematic illustration of the performance of our metadevice, which behaves as (a) a reflective lens and (e) a transmissive lens under excitations of $\hat{x}$- and $\hat{y}$-polarized waves, respectively. Top view (b) and bottom view (f) pictures of our fabricated sample. FDTD simulated profiles of (c) $\varphi^r_{xx}(x,y)$, (d) $|r_{xx}(x,y)|$, (g) $\varphi^t_{yy}(x,y)$, and (h) $|t_{yy}(x,y)|$ of the designed and fabricated metadevice. The working frequency is $f_0 = 10.6$ GHz.

where F_1 and F_2 are two focal lengths which can be freely selected. Here, still setting the working frequency as $f_0 = 10.6$ GHz, we design a full-space metalens with two focal lengths $F_1 = F_2 = 80$ mm. Different from the deflector realized in the last subsection, here the metalens does not exhibit a supercell, and thus every meta-atom should be carefully optimized such that the two phase distributions can satisfy Eq. (2). We fix the structural details of all meta-atoms adopted based on the parameter maps recorded in the Supplemental Material, Sec. B [46], and then fabricate a metalens sample according to the design, which contains 14×14 meta-atoms and has a total size of 154×154 mm^2. Figures 5(b) and 5(f) depict the top-view and bottom-view pictures of the fabricated sample. To validate our design, we calculate the distributions of two relevant phases (φ^r_{xx} and φ^t_{yy}) and amplitudes ($|r_{xx}|$ and $|t_{yy}|$) of our designed and fabricated metalens, and depict them in Figs. 5(c), 5(g), 5(d), and 5(h), respectively. Clearly, the phase profiles of the fabricated metalens follow well with the parabolic distributions dictated by Eq. (2), while the reflection and transmission amplitudes also exhibit high values ($|r_{xx}| > 0.92$ and $|t_{yy}| > 0.85$), implying the high performances of our device.

With the fabricated sample in hand, we experimentally characterize its full-space focusing performances, with reflection-mode functionality considered first. Shining the sample with an $\hat{x}$-polarized plane wave, we use a monopole antenna (~20 mm long) to measure the electric-field distributions at the reflection-side half-space. To see clearly the focusing effect, we purposely deduct the incident field from the measured total field, so that the obtained field is solely the scattered one. Figure 6(a) depicts the measured scattered-field distributions on both xoz and yoz planes at the frequency 10.6 GHz, which are normalized against the maximum value in the pattern. We find that the reflected waves are indeed well converged to a focal point at $z = -77$ mm, identified as the maximum-field point in the $|E_x|^2 \sim z$ curve along the central z axis (see Supplemental Material, Sec. G [46]). The focal length identified experimentally agrees reasonably with the theoretical value $F_1 = 80$ mm. To check the quality of the focusing effect, we quantitatively evaluate the full width at half maximum of the focal spot on the focal plane, and find it is approximately 24 mm [see inset to Fig. 6(b)]. Obviously, such a value strongly depends on the aperture size of our metalens, and can be further reduced by enlarging the total size of our lens. To identify the working bandwidth of our focusing functionality, we show in Fig. 6(b) how the measured and FDTD-computed scattered $\vec{E}$ field at the focal point varies against frequency, with the incident $\vec{E}$ field keeping as a constant. The operation bandwidth of our device, defined by the full width at half maximum of the $|E_x|^2 \sim f$ curve, is found as 0.85 GHz [shaded region in Fig. 6(b)]. Finally, we use the method reported in Refs. [24] and [38] to evaluate the working efficiency of this functionality, defined as the ratio between the powers carried by the focal spot and the incident beam. Our analysis shows that the efficiency is as high as 90.6% (see Supplemental Material, Sec. H [46]).

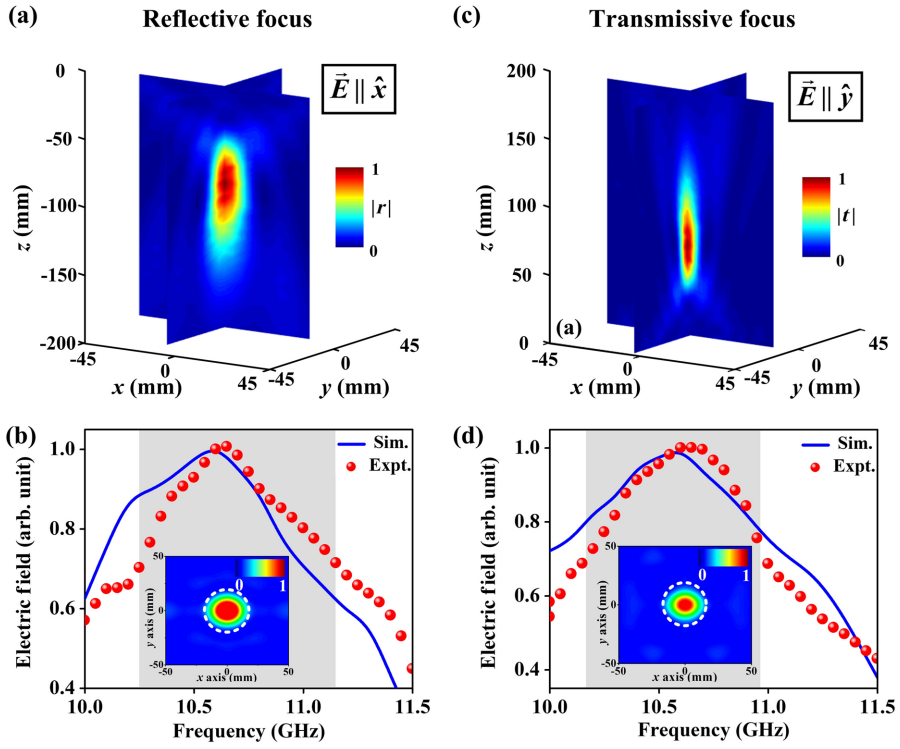

FIG. 6. Characterizations of the full-space metalens. (a) Measured $|E_x|^2$ distributions on both xoz and yoz planes at the reflection side of the metalens under illumination of normally incident $\hat{x}$-polarized wave. (b) Measured and simulated $|E_x|$ at the focal point versus frequency for our metalens under $\hat{x}$-polarized excitation. (c) Measured $|E_y|^2$ distributions on both xoz and yoz planes at the transmission side of the metalens under the illumination of normally incident $\hat{y}$-polarized wave. (d) Measured and simulated $|E_y|$ at the focal point versus frequency for our metalens under $\hat{y}$-polarized excitation. Insets to (b) and (d) depict the measured $|E_x|^2$ and $|E_y|^2$ distributions on the xy planes with $z = -77$ mm and $z = 78$ mm, respectively, with the dashed-line circles defining the sizes of the focal spots. Here, the working frequency is $f_0 = 10.6$ GHz. All field values are normalized against the maximum value in the corresponding spectrum and pattern.

We then experimentally characterize the focusing performance of our device at the transmission side of the metasurface, which is illuminated by an $\hat{y}$-polarized plane wave. The characterization procedures are essentially the same as those for the reflection-mode functionality, only with the field scanning now carried at the transmission side of the device. The measured $\vec{E}$-field distributions on both xoz and yoz planes [Fig. 6(c)] at the working frequency clearly reveal the nice focusing effect at the transmission side. The focal length is identified as 78 mm, quite close to the designed value 80 mm (see Supplemental Material, Sec. G [46]). The working bandwidth of this functionality is found as 0.75 GHz, indicated as the shaded region in Fig. 6(d), where the spectrum of the $\vec{E}$ field measured at the focal point is shown. We also check the quality of the focusing effect, and find that the size of the focal spot is about 20 mm [see inset to Fig. 6(d) for the measured field pattern on the focal plane]. Finally, we note that this focusing functionality still exhibits a high working efficiency of 85%, obtained with the same procedure as that for the reflective lens (see Supplemental Material, Sec. H [46]).

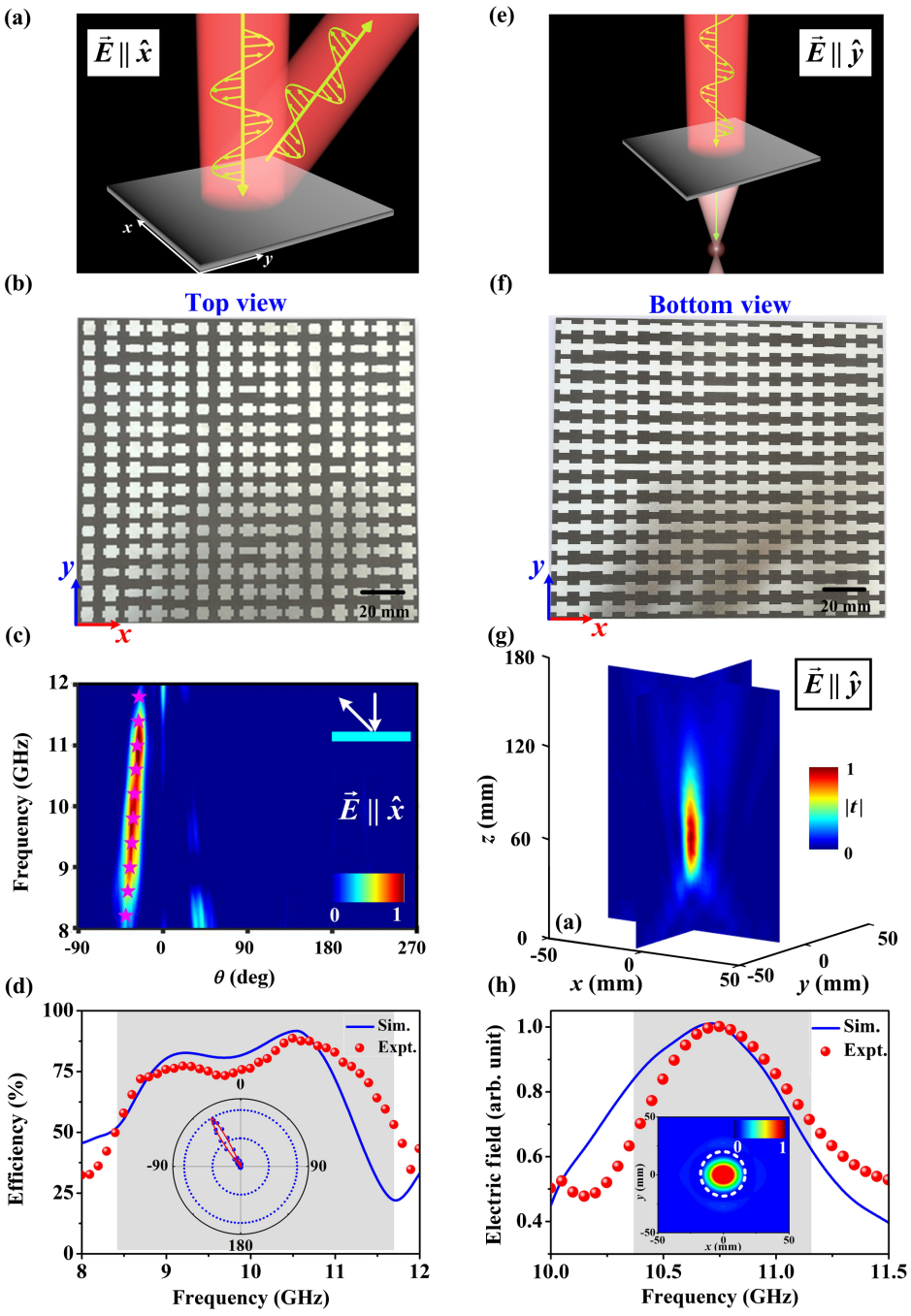

FIG. 7. Design, fabrication, and characterization of a full-space bifunctional metadevice. Schematic illustration of the performance of our metadevice, which behaves as (a) a reflective beam bender and (e) a transmissive lens under excitations of $\hat{x}$- and $\hat{y}$-polarized waves, respectively. (b) Top-view and (f) bottom-view pictures of our fabricated metadevice. (c) Measured scattered-field intensity (color map) versus frequency and detecting angle at the reflection side of the metasurface shined by normal-incidence wave with $\vec{E}||\hat{x}$ polarization. (d) Simulated and measured absolute efficiencies of the reflective beam-bending functionality of the device under $\hat{x}$-polarized excitations. Inset shows the measured and FDTD simulated scattering patterns of the metasurface. (g) Measured $|E_y|^2$ distributions on both xoz and yoz planes at the transmission side of the metasurface under illumination of normally incident $\hat{y}$-polarized wave. (h) Measured and simulated $\vec{E}$-field amplitude at the focal point as functions of frequency. Inset depicts the measured $|E_y|^2$ distributions on the xy plane with $z = 84$ mm, with the dashed-line circle defining the size of the focal spot. Here, the working frequency is 10.6 GHz and all field values are normalized against the maximum value inside each spectrum.

C. Full-space bifunctional metadevice

In previous sections, the metasurfaces that we realized exhibit the *same* functionalities for reflected and transmitted waves. In this section, we further demonstrate that such full-space manipulation is not restricted to realizing identical functionalities. As an illustration, we design a metadevice which combines beam-bending and focusing functionalities in a single device, with such two distinct functionalities working for reflected and transmitted EM waves, respectively [see Figs. 7(a) and 7(e)]. To achieve this goal, we require the two phase functions (φ^r_{xx} and φ^t_{yy}) of our metadevice to satisfy the following distributions:

$$\varphi^r_{xx}(x,y) = C_2 + \xi_3 x,$$
$$\varphi^t_{yy}(x,y) = k_0\left(\sqrt{F_3^2 + x^2 + y^2} - F_3\right), \qquad (3)$$

with C_2 being a constant. Here, ξ_3 is the phase gradient to determine the angle of the anomalously reflected wave and F_3 is the focal length for the metalens application working for the transmitted wave, both of which can be freely chosen. In our design, keeping the working frequency still at $f_0 = 10.6$ GHz, we set $\xi_3 = 0.51k_0$ and $F_3 = 85$ mm without losing generality. Aided by the structural map shown in Sec. B of the Supplemental Material [46], we optimize each meta-atom in the metasurface such that the resulting φ^r_{xx} and φ^t_{yy} distributions satisfy Eq. (3) (see Fig. S13 in the Supplemental Material, Sec. I [46]), and then fabricate a sample according to the design. Figures 7(b) and 7(f) depict the top-view and bottom-view pictures of the fabricated sample, which contains 15×15 meta-atoms and has a total size of 165×165 mm^2. Again, we emphasize that all optimized meta-atoms exhibit very high values of reflection-transmission amplitudes ($|r_{xx}| > 0.92$, $|t_{yy}| > 0.86$, see Fig. S13 in Supplemental Material, Sec. I [46]), which guarantees that our metadevice must exhibit high working efficiencies.

We first experimentally characterize the beam-bending functionality of the device at the reflection side. Following the experimental procedures described in Sec. III A, we measure the angular distributions of scattered waves in both reflection and transmission sides of the metasurface, which is shined by normally incident $\hat{x}$-polarized EM waves. Figure 7(c) clearly shows that nearly all incident powers are redirected to the anomalous-reflection angles dictated by the generalized Snell's laws (pink symbols), within a broad frequency interval (8.4–11.7 GHz). FDTD simulations reproduce the experimental observations well, and the results are presented in Sec. J of the Supplemental Material [46]. Figure 7(c) already implies that the working bandwidth of this functionality is quite broad, which is reinforced by the experimentally measured efficiency spectrum of the anomalous reflection, as shown in Fig. 7(d). Obviously, the best beam-bending performance is found at about 10.6 GHz with a peak absolute efficiency 88% (simulation result, 92%), and the inset to Fig. 7(d) shows that the scattering pattern at this frequency is very clean and contains only one single anomalous reflection mode.

We finally examine the focusing functionality of our device at its transmission side. We experimentally map out the E_y-field distributions on two high-symmetry planes at the transmission side of our metasurface, which is shined by a normally incident $\hat{y}$-polarized EM wave at 10.6 GHz. Figure 7(g) shows clearly that our metadevice now works as a metalens that can focus the transmitted wave to a focal point, with the focal length evaluated as 84 mm, agreeing well with the theoretical design ($F = 85$ mm). The spot size at the focal plane is found as 19 mm [see the inset to Fig. 7(h) for the measured field pattern on the focal plane]. Utilizing the same approach as in Sec. III B, we also experimentally characterize the working efficiency of the metalens, and find that the efficiency is roughly 85.2% (see Supplemental Material, Sec. J [46]). The measured $|E_y|$ value at the focal point is depicted in Fig. 7(h) as a function of frequency, from which we identify the working bandwidth of the metalens as 0.8 GHz (10.4–11.2 GHz).

IV. CONCLUSION

To summarize, we propose an alternative type of metasurface that can efficiently control EM wave fronts in the full space, and experimentally demonstrate the concept in the microwave regime. We design and fabricate three metadevices (with a total thickness much less than the wavelength) and experimentally demonstrate that they can simultaneously realize the beam-bending and/or focusing functionalities in transmission and reflection modes with very high working efficiencies (in the range of 85%–91%), depending on the input polarizations. Our findings open the door to realizing functional high-efficiency metadevices with full-space control abilities in different frequency domains, which are important in modern integration-optics applications.

ACKNOWLEDGMENTS

This work was supported by National Basic Research Program of China (No. 2017YFA0303504), National Natural Science Foundation of China (No. 11734007, No. 11474057, No. 11404063, No. 11674068, No. 61372034, No. 61501499, No. 11604167), Natural Science Foundation of Shanghai (No. 16ZR1445200, No. 16JC1403100), and Natural Science Foundation of Shaanxi province (No. 2016JQ6001).

[1] N. Yu and F. Capasso, Flat optics with designer metasurfaces, Nat. Mater. **13**, 139 (2014).

[2] H. Chen, A. J. Taylor, and N. Yu, A review of metasurfaces: Physics and applications, Rep. Prog. Phys. **79**, 076401 (2016).

[3] M. Born and E. Wolf, *Principles of Optics: Electromagnetic Theory of Propagation, Interference and Diffraction of Light*, 7th ed. (Cambridge University Press, Cambridge, UK, 1999).

[4] N. Yu, P. Genevet, M. A. Kats, F. Aieta, J. P. Tetienne, F. Capasso, and Z. Gaburro, Light propagation with phase discontinuities: Generalized laws of reflection and refraction, Science **334**, 333 (2011).

[5] X. Ni, N. K. Emani, A. V. Kildishev, A. Boltasseva, and V. M. Shalaev, Broadband light bending with plasmonic nanoantennas, Science **335**, 427 (2012).

[6] S. Sun, K. Yang, C. Wang, T. Juan, W. T. Chen, C. Y. Liao, Q. He, S. Xiao, W. Kung, G. Guo, L. Zhou, and D. P. Tsai, High-efficiency broadband anomalous reflection by gradient meta-surfaces, Nano Lett. **12**, 6223 (2012).

[7] S. Sun, Q. He, S. Xiao, Q. Xu, X. Li, and L. Zhou, Gradient-index meta-surfaces as a bridge linking propagating waves and surface waves, Nat. Mater. **11**, 426 (2012).

[8] W. Sun, Q. He, S. Sun, and L. Zhou, High-efficiency surface plasmon meta-couplers: Concept and microwave-regime realizations, Light Sci. Appl. **5**, e16003 (2016).

[9] A. Pors, M. G. Nielsen, T. Bernardin, J.-C. Weeber, and S. I. Bozhevolnyi, Efficient unidirectional polarization-controlled excitation of surface plasmon polaritons, Light Sci. Appl. **3**, e197 (2014).

[10] L. Huang, X. Chen, B. Bai, Q. Tan, G. Jin, T. Zentgraf, and S. Zhang, Helicity dependent directional surface plasmon polariton excitation using a metasurface with interfacial phase discontinuity, Light Sci. Appl. **2**, e70 (2013).

[11] G. Zheng, H. Mühlenbernd, M. Kenney, G. Li, T. Zentgraf, and S. Zhang, Metasurface holograms reaching 80% efficiency, Nat. Nanotechnol. **10**, 308 (2015).

[12] W. T. Chen, K. Y. Yang, C. M. Wang, Y. W. Huang, G. Sun, I. Da Chiang, C. Y. Liao, W. L. Hsu, H. T. Lin, S. Sun, L. Zhou, A. Q. Liu, and D. P. Tsai, High-efficiency broadband meta-hologram with polarization-controlled dual images, Nano Lett. **14**, 225 (2014).

[13] X. Li, L. Chen, Y. Li, X. Zhang, M. Pu, Z. Zhao, X. Ma, Y. Wang, M. Hong, and X. Luo, Multicolor 3D meta-holography by broadband plasmonic modulation, Sci. Adv. **2**, e1601102 (2016).

[14] X. Wan, X. Shen, Y. Luo, and T. J. Cui, Planar bifunctional Luneburg-fisheye lens made of an anisotropic metasurface, Laser Photonics Rev. **8**, 757 (2014).

[15] X. Chen, L. Huang, H. Mühlenbernd, G. Li, B. Bai, Q. Tan, G. Jin, C.-W. Qiu, S. Zhang, and T. Zentgraf, Dual-polarity plasmonic metalens for visible light, Nat. Commun. **3**, 1198 (2012).

[16] M. D. Huntington, L. J. Lauhon, and T. W. Odom, Subwavelength lattice optics by evolutionary design, Nano Lett. **14**, 7195 (2014).

[17] F. Aieta, M. A. Kats, and F. Capasso, Multiwavelength achromatic metasurfaces by dispersive phase compensation, Science **347**, 1342 (2015).

[18] X. Ding, F. Monticone, K. Zhang, L. Zhang, D. Gao, S. Nawaz Burokur, A. De Lustrac, Q. Wu, C. W. Qiu, and A. Alu, Ultrathin Pancharatnam–Berry metasurface with maximal cross-polarization efficiency, Adv. Mater. **27**, 1195 (2015).

[19] Z. Liu, Z. Li, Z. Liu, J. Li, H. Cheng, P. Yu, W. Liu, C. Tang, C. Gu, J. Li, S. Chen, and J. Tian, High-performance broadband circularly polarized beam deflector by mirror effect of multinanorod metasurfaces, Adv. Funct. Mater. **25**, 5428 (2015).

[20] W. Luo, S. Xiao, Q. He, S. Sun, and L. Zhou, Photonic spin Hall effect with nearly 100% efficiency, Adv. Opt. Mater. **3**, 1102 (2015).

[21] I. Yulevich, E. Maguid, N. Shitrit, D. Veksler, V. Kleiner, and E. Hasman, Optical Mode Control by Geometric Phase in Quasicrystal Metasurface, Phys. Rev. Lett. **115**, 205501 (2015).

[22] J. Hao, Y. Yuan, L. Ran, T. Jiang, J. A. Kong, C. T. Chan, and L. Zhou, Manipulating Electromagnetic Wave Polarizations by Anisotropic Metamaterials, Phys. Rev. Lett. **99**, 063908 (2007).

[23] F. Ding, Z. Wang, S. He, V. M. Shalaev, and A. V. Kildishev, Broadband high-efficiency half-wave plate: A supercell-based plasmonic metasurface approach, ACS Nano **9**, 4111 (2015).

[24] T. Cai, S. W. Tang, G. M. Wang, H. X. Xu, and S. L. Sun, High-performance bifunctional metasurfaces in transmission and reflection geometries, Adv. Opt. Mater. **5**, 1600506 (2017).

[25] S. Jia, X. Wan, D. Bao, Y. Zhao, and T. Cui, Independent controls of orthogonally polarized transmitted waves using a Huygens metasurface, Laser Photonics Rev. **9**, 545 (2015).

[26] T. Cai, G. M. Wang, X. F. Zhang, J. G. Liang, Y. Q. Zhuang, D. Liu, and H. X. Xu, Ultra-thin polarization beam splitter using 2-D transmissive phase gradient metasurface, IEEE Trans. Antennas Propag. **63**, 5629 (2015).

[27] X. Ma, M. Pu, X. Li, C. Huang, Y. Wang, W. Pan, B. Zhao, J. Cui, C. Wang, Z. Zhao, and X. Luo, A planar chiral meta-surface for optical vortex generation and focusing, Sci. Rep. **5**, 10365 (2015).

[28] D. Wen, S. Chen, F. Yue, K. Chan, M. Chen, M. Ardron, K. F. Li, P. W. H. Wong, K. W. Cheah, E. Y. B. Pun, G. Li, S. Zhang, and X. Chen, Metasurface device with helicity-dependent functionality, Adv. Opt. Mater. **4**, 321 (2016).

[29] F. Yue, D. Wen, C. Zhang, B. D. Gerardot, W. Wang, S. Zhang, and X. Chen, Multichannel polarization-controllable superpositions of orbital angular momentum states, Adv. Mater. **29**, 1603838 (2017).

[30] C. Qu, S. Ma, J. Hao, M. Qiu, X. Li, S. Xiao, Z. Miao, N. Dai, Q. He, S. Sun, and L. Zhou, Tailor the Functionalities of Metasurfaces Based on a Complete Phase Diagram, Phys. Rev. Lett. **115**, 235503 (2015).

[31] Y. Shen, D. Ye, I. Celanovic, S. G. Johnson, J. D. Joannopoulos, and M. Soljačić, Optical broadband angular selectivity, Science **343**, 1499 (2014).

[32] N. Mohammadi Estakhri and A. Alù, Wave-Front Transformation with Gradient Metasurfaces, Phys. Rev. X **6**, 041008 (2016).

[33] V. S. Asadchy, Y. Ra'Di, J. Vehmas, and S. A. Tretyakov, Functional Metamirrors Using Bianisotropic Elements, Phys. Rev. Lett. **114**, 095503 (2015).

[34] Z. Wei, Y. Cao, X. Su, Z. Gong, Y. Long, and H. Li, Highly efficient beam steering with a transparent metasurface, Opt. Express **21**, 10739 (2013).

[35] F. Monticone, N. M. Estakhri, and A. Alù, Full Control of Nanoscale Optical Transmission with a Composite Metascreen, Phys. Rev. Lett. **110**, 203903 (2013).

[36] C. Pfeiffer, N. K. Emani, A. M. Shaltout, A. Boltasseva, V. M. Shalaev, and A. Grbic, Efficient light bending with isotropic metamaterial Huygens' surfaces, Nano Lett. **14**, 2491 (2014).

[37] C. Pfeiffer, C. Zhang, V. Ray, L. J. Guo, and A. Grbic, High Performance Bianisotropic Metasurfaces: Asymmetric Transmission of Light, Phys. Rev. Lett. **113**, 023902 (2014).

[38] P. Wang, N. Mohammad, and R. Menon, Chromatic-aberration-corrected diffractive lenses for ultrabroadband focusing, Sci. Rep. **6**, 21545 (2016).

[39] M. Kenney, S. Li, X. Zhang, X. Su, T.-T. Kim, D. Wang, D. Wu, C. Ouyang, J. Han, W. Zhang, H. Sun, and S. Zhang, Pancharatnam-Berry phase induced spin-selective transmission in herringbone dielectric metamaterials, Adv. Mater. **28**, 9567 (2016).

[40] Z. Li, W. Liu, H. Cheng, J. Liu, S. Chen, and J. Tian, Simultaneous generation of high-efficiency broadband asymmetric anomalous refraction and reflection waves with few-layer anisotropic metasurface, Sci. Rep. **6**, 35485 (2016).

[41] M. Khorasaninejad, W. T. Chen, R. C. Devlin, J. Oh, A. Y. Zhu, and F. Capasso, Metalenses at visible wavelengths: Diffraction-limited focusing and subwavelength resolution imaging, Science **352**, 1190 (2016).

[42] K. Chen, Y. Feng, F. Monticone, J. Zhao, B. Zhu, T. Jiang, L. Zhang, Y. Kim, X. Ding, S. Zhang, A. Alù, and C.-W. Qiu, A reconfigurable active Huygens' metalens, Adv. Mater. **29**, 1606422 (2017).

[43] L. Zhang, S. Mei, K. Huang, and C.-W. Qiu, Advances in full control of electromagnetic waves with metasurfaces, Adv. Opt. Mater. **4**, 818 (2016).

[44] H. H. Hsiao, C. H. Chu, and D. P. Tsai, Fundamentals and applications of metasurfaces, Small Methods **1**, 1600064 (2017).

[45] F. Ding, A. Pors, and S. I. Bozhevolnyi, Gradient metasurfaces: A review of fundamentals and applications, Rep. Prog. Phys., DOI: 10.1088/1361-6633/aa8732 (2017).

[46] See the Supplemental Material at http://link.aps.org/supplemental/10.1103/PhysRevApplied.8.034033 for more discussions on the working mechanism of the meta-atom, design strategy of the full-space metasurfaces, FDTD simulation results for the full-space deflector, evaluating the working efficiencies of the full-space beam deflector, incidence-angle-dependent performance of the full-space beam deflector, estimations on the focal lengths of the full-space metalens, evaluations of the working efficiencies for the full-space metalens, phase-amplitude distributions of the full-space bifunctional metadevice studied in Fig. 7 and additional simulation and experimental data of the full-space bifunctional metadevice.